



# Enhanced radiation tolerance and plasticity in nanochannel Al<sub>0.1</sub>CoCrFeNi high-entropy alloy

Tao Cheng <sup>a,1</sup>, Wenjing Qin <sup>a,b,1</sup>, Hui Wang <sup>a</sup>, Guangxu Cai <sup>a</sup>, Suoxue Jin <sup>c</sup>, Yongqiang Wang <sup>d</sup>, Changzhong Jiang <sup>a</sup>, Feng Ren <sup>a,\*</sup>

<sup>a</sup> School of Physics and Technology, Center for Ion Beam Application, Center for Electron Microscopy and MOE Key Laboratory of Artificial Micro, and Nano-Structures, Wuhan University, Wuhan 430072, China

<sup>b</sup> School of Physics and Electronics, Hunan Normal University, Changsha 410081, China

<sup>c</sup> Institute of High Energy Physics Chinese Academy of Sciences, Beijing 430064, China

<sup>d</sup> Materials Science and Technology Division, Los Alamos National Laboratory, Los Alamos, New Mexico 87545, USA



## ARTICLE INFO

### Keywords:

High entropy alloy  
Nanochannel  
Radiation tolerance  
Strain rate sensitivity  
Plasticity

## ABSTRACT

Irradiation-induced embrittlement is a critical and common issue for nuclear materials. Here, we find that the structural design of high-entropy alloy (HEA), nanochannel Al<sub>0.1</sub>CoCrFeNi HEA, not only enhances the irradiation tolerance, but also significantly relieves the irradiation-induced embrittlement. We present a systematic investigation on the irradiation tolerance and the mechanical response of the nanochannel HEA irradiated by 40 keV He<sup>+</sup> ions to the fluence of 5 × 10<sup>17</sup> ions/cm<sup>2</sup> and by 2 MeV Ar<sup>+</sup> ions to a fluence of 6 × 10<sup>16</sup> ions/cm<sup>2</sup>. It is uncovered that the nanochannel HEA exhibits better He management ability and radiation damage tolerance than its dense counterpart. Furthermore, nanoindentation tests show that the irradiated nanochannel HEA has a better mechanical response compared with its dense counterpart: (1) Strain rate sensitivity (SRS) exponent (*m*) of the nanochannel HEA has only a slight decrease compared to the large decrease for the dense HEA; and (2) the SRS exponent (*m*) of the nanochannel HEA is elevated while that of the dense HEA is consistently decrease after He<sup>+</sup> ion irradiation. These results highlight that nanochannel structure with enormous free surface can mitigate the deleterious effects of irradiation as comparing with its dense counterpart, and represents a new promising strategy to design radiation tolerant materials for the advanced nuclear reactor systems.

## 1. Introduction

In the future advanced nuclear reactor systems, the interaction of fast neutron with materials not only introduces large numbers of damage defects, but also produces a great amount of transmutation products such as hydrogen (H) or helium (He) gas. Irradiation-induced degradation in microstructural and mechanical properties of materials, as evidenced by swelling, hardening and embrittlement, can be quite obvious [1]. Thus, the development of novel materials with outstanding radiation tolerance is of great significance. Numerous studies have revealed that grain boundaries and interfaces can act as “sinks” to trap defects and “sources” to annihilate defects nearby [2,3]. However, taking the He<sup>+</sup> ion irradiation as an example, although such grain boundaries or interfaces can effectively improve the ability to store He atoms, cracking at the grain boundaries or interfaces is inevitable after introducing high

fluence of gas atoms, which suggests that their capability for storing bubbles is still limited [4]. As irradiation-induced embrittlement is a critical and common issue for nuclear materials, designing embrittlement-resistant material through material composition and microstructure tailoring is an urgent task.

High-entropy alloys (HEAs) are attracting wide academic interest due to their unique structures and excellent properties such as promising radiation tolerance, simultaneous strength and ductility, fatigue resistance compared with conventional alloys [5–9]. Thus, HEAs have been proposed as promising candidates for radiation tolerant cladding for nuclear fuel, damage tolerance materials at cryogenic temperatures or structural materials in the next generation of advanced nuclear reactor systems [6,10]. The intrinsic mechanisms of HEAs with high radiation tolerance such as the correlations of compositional complexity on the irradiation response have been extensively studied. For example, Lu

\* Corresponding author.

E-mail address: [fren@whu.edu.cn](mailto:fren@whu.edu.cn) (F. Ren).

<sup>1</sup> Contributed equally to this work.

et al. explored the radiation performances of single-phase concentrated solid solution alloys in high energy  $\text{Ni}^+$  irradiation, and concluded that the increased chemical disorder contributes to tailoring the motion of interstitial defect clusters and improves the swelling resistance [11]; Yang et al. found that the irradiated  $\text{Al}_{0.1}\text{CoCrFeNi}$  HEA by 3 MeV Au ions in elevated temperatures induced enrichment of Ni and Co and depletion of Fe and Cr at defect clusters [12]; Wang et al. discovered that the Pd element was better than Mn in suppressing of void swelling and dislocation loop growth by comparing the irradiation response of NiCoFeCrMn and NiCoFeCrPd HEAs [13]. However, there is still irradiation hardening in FeNiMnCr and W-Ta-V-Cr HEAs [14,15]. It is even better if we could design a nanostructured HEA material with the ability to transform irradiated-introduced He from a disadvantage to an asset, to improve the post-irradiation mechanical performance in such material.

In recent years, a new strategy has been reported through intentionally engineering nanochannel structures to absorb and release irradiation-induced gas atoms and defects out of materials rather than absorbing and storing them into the materials [4,16]. It was found that the increase of hardness in the nanochannel tungsten films is lower than that of bulk tungsten after He ion irradiation because the nanochannel structures can release He atoms to suppress rapid He built-up [16–18]. Moreover, the nanochannel structures can also alleviate the accumulation of stress by releasing the dislocations induced by plastic deformation when subjected to large thermal shock [19]. From all the above, it is practicable to fabricate a nanochannel structural HEA material with excellent radiation tolerance and enhanced post-irradiation mechanical performance upon  $\text{He}^+$  ions irradiation.

In this work, we introduced the nanochannel structure into the  $\text{Al}_{0.1}\text{CoCrFeNi}$  HEA with a face-centered cubic (FCC) single phase. The irradiation resistance performances of the HEA films were explored by being irradiated by 40 keV  $\text{He}^+$  ions to the fluence of  $5 \times 10^{17}$  ions/cm<sup>2</sup> and 2 MeV  $\text{Ar}^+$  ions to  $6 \times 10^{16}$  ions/cm<sup>2</sup>, respectively. Furthermore, we also focused on the relationship between the mechanical response of the irradiated nanochannel structure in terms of strain rate sensitivity (SRS) and the evolution of irradiation-induced microstructure, where the influence of microstructure on the plasticity response of irradiated HEAs is still less studied.

## 2. Experimental

### 2.1. Materials preparation

Two different  $\text{Al}_{0.1}\text{CoCrFeNi}$  HEA films were deposited on silicon (100) substrates using an ultrahigh vacuum magnetron sputtering system (ULVAC, ACS-4000-C4) under selected deposition conditions: the one with nanochannel structures was deposited by DC power supply in room temperature (RT) and named as nanochannel  $\text{Al}_{0.1}\text{CoCrFeNi}$  HEA film (nanochannel HEA); the other without nanochannel structures was deposited by RF power supply at 500 °C and named as dense  $\text{Al}_{0.1}\text{CoCrFeNi}$  HEA film (dense HEA). The  $\text{Al}_{0.1}\text{CoCrFeNi}$  high entropy alloy target was prepared by metallurgy with high purity raw materials (>99.99%) of cobalt (Co), chromium (Cr), iron (Fe), nickel (Ni), and aluminum (Al). In order to compare the  $\text{He}^+$  ion irradiation tolerance performance of  $\text{Al}_{0.1}\text{CoCrFeNi}$  HEA films with the commercial product, bulk reduced activation ferritic/martensitic steels (RAFM) with dimensions of 10 mm × 10 mm × 1 mm were also studied.

### 2.2. Ion irradiation

To quantitatively study the He distribution in the  $\text{Al}_{0.1}\text{CoCrFeNi}$  HEA films, well-controlled ion implantation processes were used to investigate the He retention and the bubble formation behaviors. The  $\text{Al}_{0.1}\text{CoCrFeNi}$  HEA films with 1 μm thickness and the bulk RAFMs were bombarded by a 40 keV  $\text{He}^+$  ion beam to the fluences of  $3 \times 10^{17}$  and  $5 \times 10^{17}$  ions/cm<sup>2</sup> at RT using a 200 keV ion implanter (LC22-100-01) in Centre for Ion Beam Application, Wuhan University. The corresponding

ion range and displacement per atom (dpa) on  $\text{Al}_{0.1}\text{CoCrFeNi}$  HEA (see Fig. S1a) were calculated using SRIM 2013 with a simple Kinchin-Pease method [20], the displacement energies for different atoms were all set as 40 eV [21]. For the given  $\text{He}^+$  ion energy (40 keV) and fluence ( $5 \times 10^{17}$  ions/cm<sup>2</sup>), SRIM results predict that the peak He concentration is 41.2 at% at the depth of 170 nm and the maximum dpa is 15.0 at the depth of 130 nm in the  $\text{Al}_{0.1}\text{CoCrFeNi}$  HEA; as for RAFMs, the peak He concentration is almost identical (41.7 at% at the depth of 170 nm) to the  $\text{Al}_{0.1}\text{CoCrFeNi}$  HEA, and the maximum dpa is 21.7 at the depth of 140 nm (Fig. S1b).

The  $\text{Al}_{0.1}\text{CoCrFeNi}$  HEA films were also irradiated by 2 MeV  $\text{Ar}^+$  ions to the fluence of  $6 \times 10^{16}$  ions/cm<sup>2</sup> at 500 °C on a 4UH pelletron accelerator (National Electrostatics Corporation) in the Key Laboratory of Nuclear Radiation and Nuclear Energy Technology, Chinese Academy of Sciences (CAS). The ion current was maintained at 0.3 uA/cm<sup>2</sup> to avoid beam-heating of samples. The maximum damage is 43.2 dpa at the depth of 670 nm obtained from the SRIM results (Fig. S2). To allow the energetic ions to penetrate the film and avoid repeated collision with the matrix atoms, the  $\text{Al}_{0.1}\text{CoCrFeNi}$  HEA films with a thickness of 550 nm were used for high-energy ion irradiation.

### 2.3. Characterization method

Cross-sectional transmission electron microscopy (XTEM) images of the pristine and irradiated samples were performed using JEOL JEM-2100 and JEM-2010 (HT) (TEM) operating at 200 kV. The TEM samples were prepared using standard cross-sectioning technique, including mechanical grinding, polishing, dimpling and ion milling procedures. The samples were mechanical grinded and polished to approximately 40 μm by abrasive paper using the Gatan precision disc grinder, then dimpled to approximately 20 μm, and finally thinned to electron transparency using a Gatan Precision Ion Polishing System. All the TEM images were imaged in similar under-focus values. Crystalline structures of the as-deposited  $\text{Al}_{0.1}\text{CoCrFeNi}$  HEA films were identified by grazing incidence X-ray diffraction (a Rigaku SmartLab 9 kW X-ray diffractometer with Cu  $\text{K}\alpha$  radiation) with tilting angle of 0.5°. Doppler broadening spectroscopy (DBS) based on slow positron beam was carried at the Institute of High Energy Physics, Chinese Academy of Sciences to detect and analyze the distribution of open volume defects in the  $\text{Al}_{0.1}\text{CoCrFeNi}$  HEA films, in which the  $S$  parameter is defined as the ratio of the central low momentum area of the spectrum (510.2–511.8 keV) to the total spectrum (499.5–533.5 keV). The selected incident positron energy range was 0.18–20.18 keV. In addition, the changes of nano-indentation hardness and strain rate sensitivity (SRS) exponent ( $m$ ) of the pristine and irradiated  $\text{Al}_{0.1}\text{CoCrFeNi}$  HEA films were measured by using continuous stiffness measurement (CSM) mode on a Nano Indenter G200 with a standard Berkovich tip at RT. Three different loading strain rates (0.005, 0.01 and 0.05 s<sup>-1</sup>) were chosen for the test. All nano-indentation data were extracted within an indentation depth of 10–20% of the film thickness for each sample to eliminate substrate effects. More than 12 indents separated from each other of ~50 μm were performed on each sample, and at least 8 effective data were involved in eventual analysis.

## 3. Results and discussion

### 3.1. Microstructure of the pristine HEA films

Cross-sectional TEM (XTEM) images of the pristine nanochannel and dense  $\text{Al}_{0.1}\text{CoCrFeNi}$  HEA films (named nanochannel HEA and dense HEA, respectively) are presented in Figs. 1a-1b. The surface SEM images of the nanochannel HEA and dense HEA film are shown in Fig. S3. The nanochannel and dense HEA films consist of apparent columnar crystals along the grain growth direction and the average column sizes obtained by taking statistical measurements from several XTEM images are  $33 \pm 11$  and  $86 \pm 27$  nm, respectively. Notably, nanochannels with open

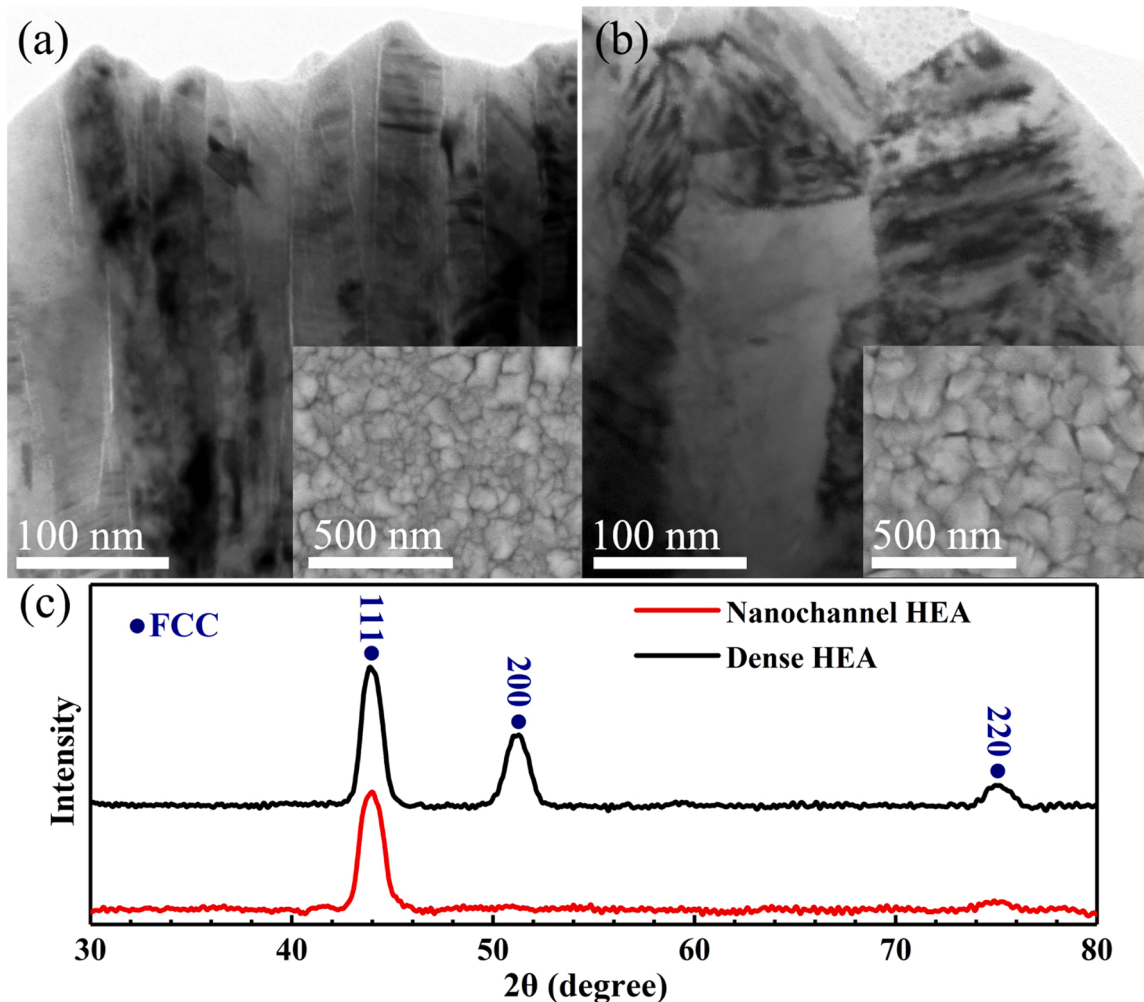


**Fig. 1.** XTEM and planar SEM images of the pristine (a) nanochannel HEA, (b) dense HEA and (c) the corresponding GIXRD diffraction patterns.

space between columnar crystals are successfully fabricated in the nanochannel HEA deposited under DC sputtering, while no detectable open boundaries are found in the dense HEA deposited under RF sputtering. GIXRD results (Fig. 1c) show that the diffraction pattern of nanochannel and dense HEA possess only a strong {111} peak, and the dense HEA has other two relative weak peaks {200} and {220}, indicating that these two kinds of films are all FCC phase. Different magnetron deposition conditions lead to different structural characteristics and preferred orientations between the nanochannel HEA and dense HEA. The preferred orientation growth of columnar crystal with nanochannel structures during RT deposition is via the mechanism of Zone T in the well-known structure zone models (SZM), where limited surface atom diffusion, the wide angular distribution of the deposition flux and atomic shadowing effect play the key roles [22,23]. While for the dense HEA, the high deposition temperature (500 °C) and the additional self-bias effect produced by RF power improve the kinetic energy of energy particles reaching the deposited surface, enhance the surface atom migration and diffusion, which inhibit the formation of nanochannels and significantly increase the columnar crystal size in the film. Full migration and diffusion of surface atoms greatly affects the structure and morphology of the film and accelerates the growth of the film to different preferred orientation [24].

### 3.2. He management ability of the HEA films

To study the He behaviors in the Al<sub>0.1</sub>CoCrFeNi HEA films, samples are irradiated by 40 keV He<sup>+</sup> ions to the fluences of  $3 \times 10^{17}$  and

$5 \times 10^{17}$  ions/cm<sup>2</sup>. Meanwhile, the bulk RAFMs is selected as contrast sample irradiated to the fluence of  $5 \times 10^{17}$  ions/cm<sup>2</sup>. Visible He bubbles with Gaussian-distributed along the irradiation depth are formed in both HEA films, as shown in Fig. 2. The inset images are all obtained from the region of peak He concentration (with a depth of about 170 nm). The He bubbles are relatively small under irradiation to  $3 \times 10^{17}$  ions/cm<sup>2</sup>, and become larger with the increase of fluence to  $5 \times 10^{17}$  ions/cm<sup>2</sup> (corresponding to a peak He concentration of 41.2 at %). No cracks are found at such a high fluence ( $5 \times 10^{17}$  ions/cm<sup>2</sup>) in any of the Al<sub>0.1</sub>CoCrFeNi HEA films. However, ~15 nm-wide cracks parallel to the sample surface are observed in the bulk RAFMs (Fig. 2c<sub>2</sub>) near the peak He concentration area under the same irradiation condition. Clearly, the growth of He bubbles in the nanochannel HEA and the dense HEA is greatly suppressed, and no cracks are found. Cracks in the bulk RAFMs are formed through lateral coalescence and growth of spherical He bubbles. These results suggest that the Al<sub>0.1</sub>CoCrFeNi HEA films have a better ability in suppressing the formation and growth of He bubble than the bulk RAFMs. The better He management ability in the Al<sub>0.1</sub>CoCrFeNi HEA films should be mainly attributed to its intrinsic properties. The severe lattice distortion effects in HEAs could impede He atoms or vacancies diffuse into He/vacancy clusters or He bubbles, because the migration energy of He is high and the diffusion of He atoms is relatively difficult in HEAs compared with traditional fcc metallic materials, resulting in the suppression of He bubbles formation and growth [25]. In addition, the enhanced point defect recombination in HEAs also results in a lower vacancy concentration for He bubble formation and growth [11,26]. Finally, the nano-structure in the

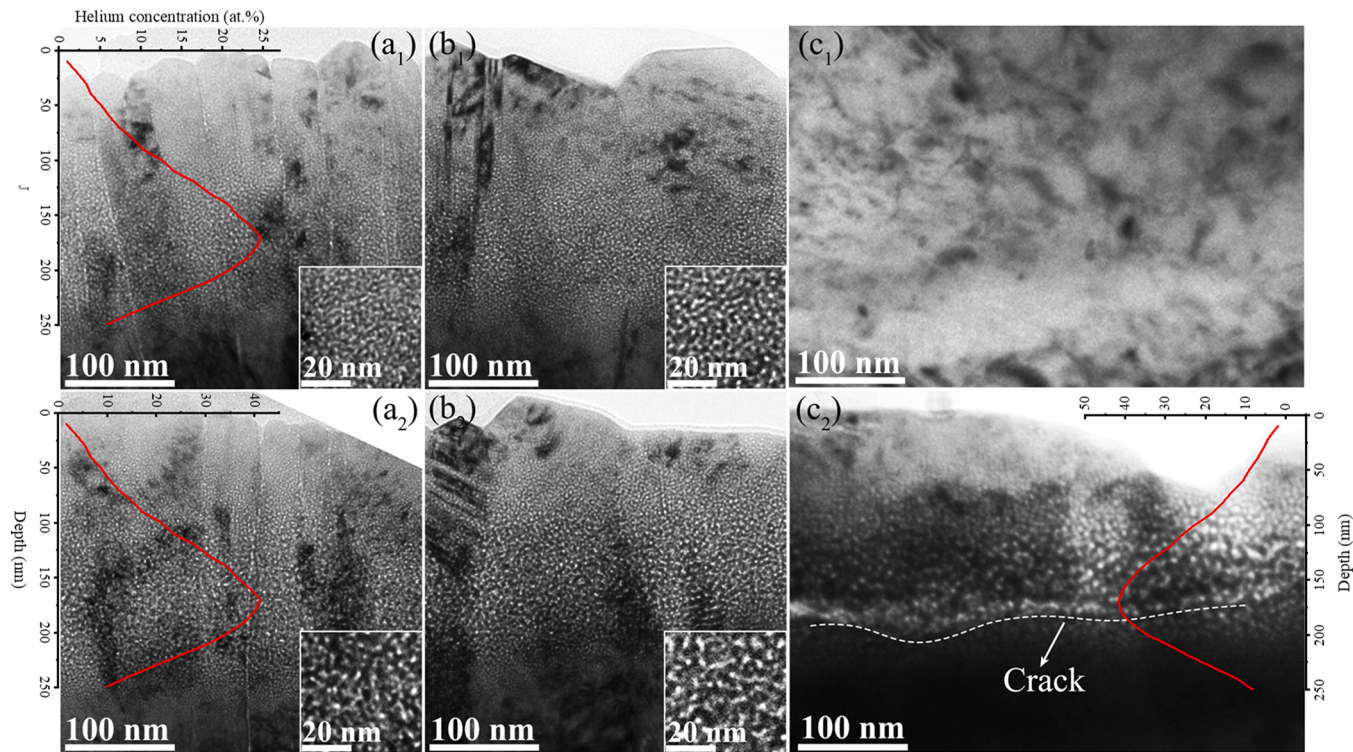


**Fig. 2.** XTEM images of the (a) nanochannel HEA and the (b) dense HEA irradiated by 40 keV  $\text{He}^+$  ions to the fluences of (a<sub>1</sub>-b<sub>1</sub>)  $3 \times 10^{17}$  and (a<sub>2</sub>-b<sub>2</sub>)  $5 \times 10^{17}$  ions/ $\text{cm}^2$ , respectively. Inserts are the magnified images of He bubbles from the peak He concentration positions. XTEM images of bulk RAFMs (c<sub>1</sub>) before and (c<sub>2</sub>) after irradiation by 40 keV  $\text{He}^+$  ions to a fluence of  $5 \times 10^{17}$  ions/ $\text{cm}^2$ . The relative He concentrations of HEA and RAFMs calculated by SRIM with depth are shown in the red lines in (a<sub>1</sub>, a<sub>2</sub> and c<sub>2</sub>).

$\text{Al}_{0.1}\text{CoCrFeNi}$  HEA films also plays a role in enhancing its He management ability.

It should be noted the nanochannel HEA and the dense HEA exhibit different responses in terms of He bubble size and distribution after  $\text{He}^+$  ion irradiation, as illustrated in Fig. 3. The average He bubble sizes in the region near the peak He concentration of the  $3 \times 10^{17}$   $\text{He}^+$  ions/ $\text{cm}^2$  irradiated nanochannel HEA and the dense HEA are  $1.13 \pm 0.16$  and  $1.64 \pm 0.21$  nm, respectively. They continually grow to  $1.35 \pm 0.27$  and  $1.86 \pm 0.31$  nm as the fluence increase to  $5 \times 10^{17}$  ions/ $\text{cm}^2$ . It also should be noted that the maximum He bubble size in the dense HEA is 3.4 nm in diameter, while it is only 2.2 nm in the nanochannel HEA. In addition, the He bubble area density of the nanochannel HEA ( $4.96 \times 10^{12}$   $\text{cm}^{-2}$ ) is slightly higher than that of the dense HEA ( $4.4 \times 10^{12}$   $\text{cm}^{-2}$ ) irradiated to the fluence of  $5 \times 10^{17}$  ions/ $\text{cm}^2$ . These results suggest that the He concentration in the nanochannel HEA is lower than that in the dense HEA. During the  $\text{He}^+$  ion irradiation, due to the low solubility of He in metals, the incident He atoms are easily trapped by vacancies to form bubble nucleus. With the increase of incident He atom number, the He bubble nucleus gradually grows into He bubbles by absorbing more He atoms and vacancies [27,28]. Our recent studies have demonstrated that, compared with secondary phase or grain boundaries, nanochannel structure with a giant free surface to volume ratio can effectively help He release and therefore decrease He concentration and suppress He bubble formation and growth during  $\text{He}^+$  ion irradiation [16,29,30]. These results clearly indicate that the nanochannel HEA exhibits better He management ability than its dense counterpart. Based on the experimental observations, it could hypothesize that the nanochannel structure with rich free surfaces can effectively absorb He atoms from the matrix and then release them into the nanochannels during  $\text{He}^+$  ion irradiation. In short, the nanochannel HEA has better  $\text{He}^+$  ion irradiation tolerance, particularly in effectively mitigating high levels of He and managing He bubbles compared with its dense counterpart and the bulk RAFMs.

### 3.3. Radiation damage tolerance of the HEA films

To explore the radiation damage tolerance of the  $\text{Al}_{0.1}\text{CoCrFeNi}$  HEA films, the nanochannel HEA and the dense HEA are irradiated at 500 °C by 2 MeV  $\text{Ar}^+$  ions to a fluence of  $6 \times 10^{16}$  ions/ $\text{cm}^2$  (~ 43.2 dpa of maximum damage). Due to the limited viable ion energy of irradiated  $\text{Ar}^+$  ions, the deposited thickness of the nanochannel HEA and the dense HEA are selected to around 550 nm to avoid the remaining of Ar atoms in the irradiated region to form Ar bubbles. Fig. 4 shows the XTEM images and corresponding HRTEM images of the irradiated nanochannel HEA and dense HEA with a depth range of 200–500 nm from the surface. The damage in this region is in the range of 16.5 – 32.2 dpa. Clearly, no visible void is found in these two samples at such high irradiation damage. The nanochannels in the nanochannel HEA still exist and are not occupied by the irradiation-induced defects. Due to the small columnar crystal size, it is impossible to observe the specific distribution of dislocations in these two irradiated samples by rotating the crystal band axis. Hence, to further explore the small-sized defects distribution, a powerful method of doppler broadening spectroscopy (DBS) was used to probe the distribution of open volume defects in these samples. The DBS with variable incident positron energy exhibits a high sensitivity to the open volume defects of the crystalline lattice, such as vacancies, dislocations, free surfaces and grain boundaries, etc [31]. Positrons are easily trapped by the open volume defects and then annihilated by valence electrons with low momentum, resulting in a narrowing of the DBS peak and improving the *S* parameter. Thus, the *S* parameter is to characterize the proportion of positron annihilated by valence electron with low momentum [32].

Fig. 5 shows the *S* parameter of the pristine and irradiated nanochannel HEA and dense HEA as a function of positron energy and corresponding mean depth. The mean depth of the positron annihilation (*R*, nm) is calculated by the following empirical formula:

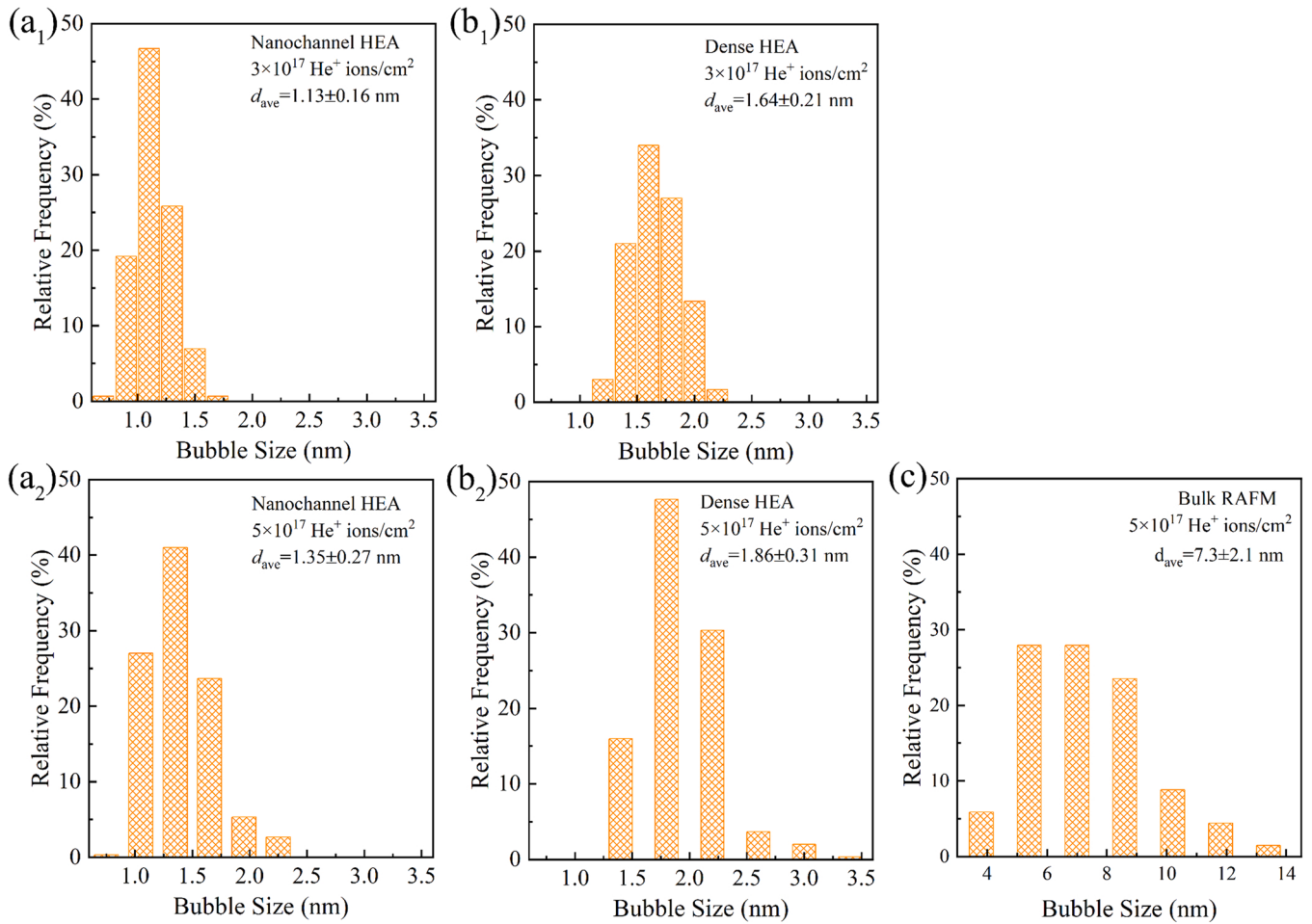


**Fig. 3.** Statistical results of the He bubble size near the peak He concentration in the (a) nanochannel HEA, (b) dense HEA and (c) bulk RAFMs irradiated by 40 keV  $\text{He}^+$  ions to a fluence of (a<sub>1</sub>, b<sub>1</sub>)  $3 \times 10^{17}$  and (a<sub>2</sub>, b<sub>2</sub>, c)  $5 \times 10^{17}$  ions/ $\text{cm}^2$ , respectively.

$$R = (40/\rho)E^{1.6} \quad (1)$$

where  $\rho$  is the density of material ( $\text{g}/\text{cm}^3$ ),  $E$  is the incident positron energy (keV) [33]. Obviously, the selected incident positron energies (0.18–20.18 keV) can probe the whole film. For the pristine samples, the  $S$  parameter of the nanochannel HEA and dense HEA gradually increases with the increase of depth, this is because both the nanochannel (free surface) and grain boundary in the nanochannel HEA and dense HEA are the open volume defects and their densities increase with the depth. Moreover, it is clear to see that the  $S$  value of the nanochannel HEA is always greater than that of the dense HEA in any depth, resulting from two main factors: one is that the room temperature deposited nanochannel HEA has more intrinsic defects than the high temperature deposited dense HEA, and another is that the column size of the nanochannel HEA is smaller than that of the dense HEA, that is, the density of nanochannels is higher than that of grain boundaries in the dense HEA. While for the irradiated samples, the  $S$  parameters are increased substantially compared with the pristine ones since the large amounts of open volume defects such as vacancies or other defects are formed during the  $\text{Ar}^+$  ion irradiation. Specifically, the variation trends of  $S$  parameters in the pristine and irradiated nanochannel HEA are almost similar. The  $S$  parameter of the irradiated dense HEA is greatly increased on the surface and showed a downward trend near a depth of 65 nm and then continued to gradually increase. The huge enhancement in the  $S$  value near the surface is because the positrons can easily scatter back to the surface as well as formation energy of the open volume defects is relatively low near the surface [33]. In addition, unexpectedly, the  $S$

value of the irradiated nanochannel HEA is much lower than that of irradiated dense HEA at the same fluence, that is, the increment of  $S$  value induced by irradiation in the dense HEA is much higher than that of the nanochannel HEA, which indicates that the open volume defects induced by irradiation in the dense HEA are greater than those in the nanochannel HEA. It shows that nanochannels can absorb and annihilate irradiation-induced defects. Hence, the nanochannel HEA has better radiation damage tolerance performance than the dense HEA during the  $\text{Ar}^+$  irradiation.

#### 3.4. Mechanical response of the HEA films to irradiation

Defects produced by irradiation will inevitably affect the mechanical properties of the  $\text{Al}_{0.1}\text{CoCrFeNi}$  HEA films. The original CSM nano-hardness curves of all the samples before and after irradiated by high-energy  $\text{He}^+$  and  $\text{Ar}^+$  ions are shown in Figs. S4–S6. Fig. 6a shows the nanoindentation hardness evolutions of the nanochannel HEA and dense HEA irradiated by 40 keV  $\text{He}^+$  ions to the fluences of  $3 \times 10^{17}$  and  $5 \times 10^{17}$  ions/ $\text{cm}^2$  or by 2 MeV  $\text{Ar}^+$  ions to  $6 \times 10^{16}$  ions/ $\text{cm}^2$ . The average hardness at different strain rates is listed in table S1. For the pristine samples, the hardness of the nanochannel HEA is larger than that of the dense HEA, and the hardness values increase with the decrease of the film thickness. According to the Hall-Petch relation, the smaller grain size will lead to a greater hardness due to the obstruction of dislocation movement by grain boundaries. Similarly, nanochannels also can hinder the migration of dislocations, leading to an increase in hardness [34]. Clearly, the nanochannel HEA and dense HEA are

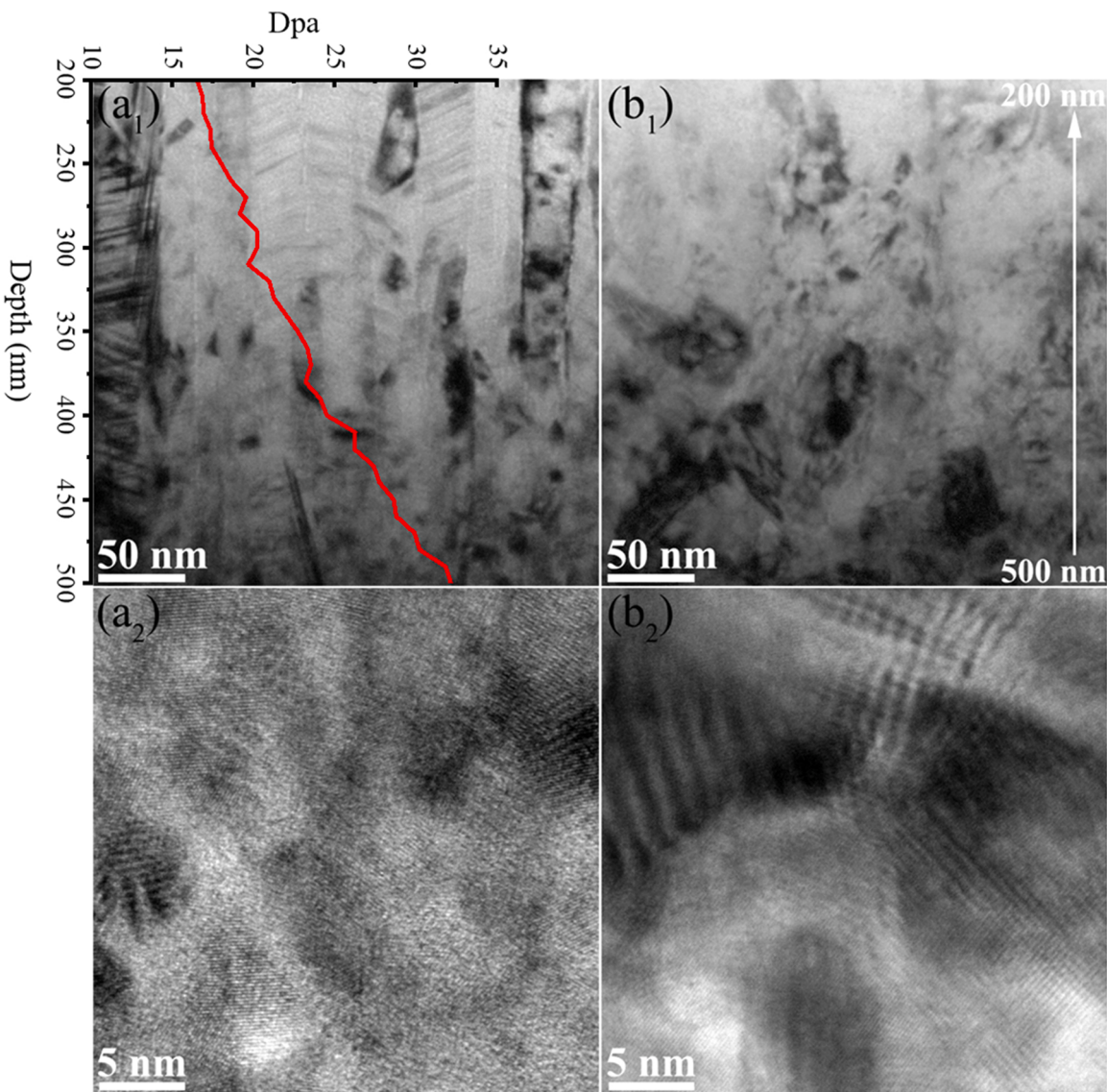


**Fig. 4.** XTEM images ( $a_1$ - $b_1$ ) and corresponding HRTEM images ( $a_2$ - $b_2$ ) of the nanochannel HEA (a) and dense HEA (b) irradiated by 2 MeV  $\text{Ar}^+$  ions to the fluence of  $6 \times 10^{16}$  ions/ $\text{cm}^2$  at 500 °C. The dpa of HEA calculated by SRIM with depth are shown in the red line in ( $a_1$ ).

observed with hardening at the fluence of  $3 \times 10^{17}$  ions/ $\text{cm}^2$  and softening at  $5 \times 10^{17}$  ions/ $\text{cm}^2$  after the  $\text{He}^+$  ions irradiation. Moreover, the hardness value of the nanochannel HEA irradiated at  $5 \times 10^{17}$  ions/ $\text{cm}^2$  is much lower than that of the pristine one. Besides, apparently irradiation-induced hardening is also found in the nanochannel HEA and dense HEA irradiated by 2 MeV  $\text{Ar}^+$  ions at high temperature, and the increase of hardness in the nanochannel HEA is slightly lower than that of the irradiated dense HEA.

SRS is often employed to characterize the strain-rate effect on the mechanical responses of material. The corresponding SRS exponent ( $m$ ) is usually used to determine the likely deformation mechanisms of material because it can quantitatively measure the sensitivity of flow stress to the loading rate, and the larger  $m$  value generally implies better plasticity [35,36]. Moreover, it is well known that the SRS of metallic materials is greatly dependent on the grain size, and the variation of SRS with grain size (or thickness) can be explained by the transition of deformation mechanisms associated with dislocation activities [37]. The SRS exponent ( $m$ ) is experimentally defined as the double logarithmic plot slope of hardness ( $H$ ) and strain rates ( $\dot{\epsilon}$ ) under isothermal conditions, specifically expressed as follows [38]:

$$m = \frac{\partial \ln H}{\partial \ln \dot{\epsilon}} = \frac{3\sqrt{3}k_B T}{V^* H} = \frac{\sqrt{3}k_B T}{V^* \sigma} \quad (2)$$

where  $k_B$  is the Boltzmann constant,  $T$  is the absolute temperature,  $\sigma$  is the flow stress,  $H$  is the hardness,  $V^*$  is the activation volume for plastic deformation which shed light on the thermally activated physical mechanism of deformation, that can be described as:

$$V^* = b \times \xi \times l^* \quad (3)$$

where  $b$  is the Burger vector of the activated dislocation,  $\xi$  is the distance swept out by mobile dislocation during one thermal activation event, and  $l^*$  is the Friedel sampling length that scales with the average contact distance between two obstacles, and when the controlling length scale at very small grain size,  $l^* = Cd$ ,  $C$  is proportionality factors [38,39].

The flow stress ( $\sigma$ ) which contributions from both grain boundaries and dislocations can be estimated as:

$$\sigma = \frac{1}{3}H = \sigma_0 + \alpha\sqrt{\rho} + \frac{\beta}{\sqrt{d}} \quad (4)$$

where the first term accounts for the lattice friction and solid solution

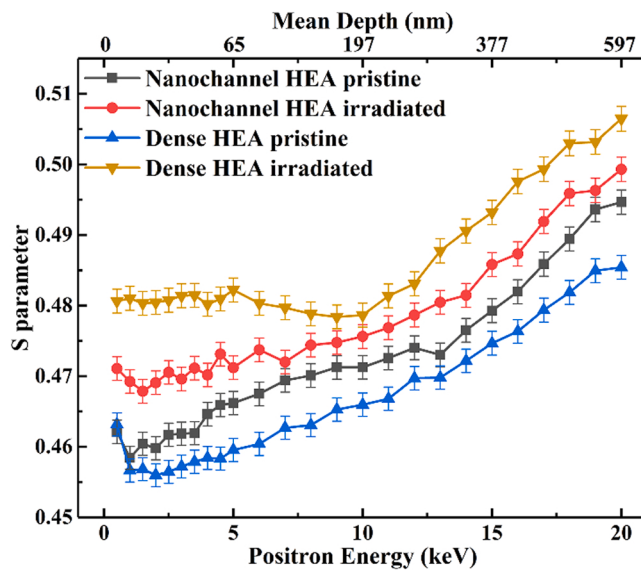


**Fig. 5.**  $S$  parameter as a function of positron energy and corresponding mean depth in the pristine nanochannel HEA and dense HEA irradiated by 2 MeV  $\text{Ar}^+$  ions to the fluence of  $6 \times 10^{16}$  ions/ $\text{cm}^2$  at 500 °C.

strength, the second term comes for Taylor contribution, and the third arises from the Hall-Petch relationship.  $\rho$  is dislocation density,  $d$  is the mean grain size,  $\alpha$  and  $\beta$  are the proportionality factors [39–41].

Combined with the above equations, the SRS exponent ( $m$ ) becomes that:

$$m = \frac{\sqrt{3k_B T}}{b\xi C(\sigma_0 d + \alpha\sqrt{\rho d} + \beta\sqrt{d})} \quad (5)$$

Clearly, for the pristine samples, the  $m$  value decreases with the decrease of the film thickness.

The SRS exponent ( $m$ ) obtained by Eq. (2) of the nanochannel HEA and dense HEA before and after irradiation are listed in table S2 and plotted in Fig. 6b (see note 1 in supplementary materials for details). The  $m$  values of the pristine nanochannel HEA and dense HEA with 1  $\mu\text{m}$  thickness are 0.03021 and 0.048, respectively, and the pristine nanochannel HEA and dense HEA with 550 nm thickness are 0.02307 and 0.03975, respectively. After the  $\text{He}^+$  ion irradiation, it is found that the  $m$  values of the nanochannel HEA (0.02504) and dense HEA (0.03816) are significantly reduced at the fluence of  $3 \times 10^{17}$  ions/ $\text{cm}^2$  compared to those of pristine ones. However, at the fluence of  $5 \times 10^{17}$  ions/ $\text{cm}^2$ ,

the  $m$  value of the dense HEA (0.03131) continued to decrease, while the  $m$  value of the nanochannel HEA (0.03166) increased. Similarly, the  $m$  values are decreased in both the nanochannel HEA and dense HEA after the  $\text{Ar}^+$  ion irradiation, and the  $m$  value reduction for the dense HEA is larger than that of the nanochannel HEA.

Meanwhile, it is odd to find that, as the column size reduced from 86 nm (dense HEA) to 33 nm (nanochannel HEA), the  $m$  value of nanochannel HEA is reduced rather than increased compared with the dense counterpart. The reason for this can be explained as follows: because the columns in the nanochannel HEA are surrounded by nanochannels, the plastic deformation of columns during nanoindentation can occur without the distortion of neighboring columns as in the dense HEA [42]. As dislocations are the main carrier of plastic deformation, dislocation sources will be required to reach the plastic deformation. For the nanochannel film with numerous free surfaces, the dominant plasticity mechanism would be surface nucleation of dislocations [43]. It is observed that dislocations quickly annihilate at free surfaces at a faster rate than they nucleate [44,45]. In this scenario, the required flow stress has to increase to sustain the strain, which is so-called “hardening by dislocation starvation” [46]. Besides, the presence of nanochannel irregularities in the nanochannel HEA (the nanochannels are not absolutely perpendicular to the substrate from surface to bottom, as shown in Fig. 1) would result in stress concentration at such irregularities [42]. With these above two factors, the stress level of the nanochannel HEA during nanoindentation can be much greater than that applied to the dense HEA. Consequently, the hardness of the nanochannel HEA is larger than that of dense HEA, and this is more pronounced at the 550 nm thickness. The  $m$  value of the nanochannel HEA calculated by Eq. (2) corresponds to the increased stress level which is smaller than that of the dense HEA.

The  $\text{Al}_{0.1}\text{CoCrFeNi}$  HEA films subjected to heavy  $\text{Ar}^+$  ion irradiation usually lead to large amounts of vacancies or dislocations formation. No visible nanovoids are found in Fig. 4, suggesting that the irradiation-induced small defects can act as strong obstacles that impede dislocation motion, resulting in a large increase in hardness and a greatly reduction in plasticity. However, it is noteworthy that the nanochannel HEA has alleviative irradiation-induced embrittlement after  $\text{Ar}^+$  ion irradiation concluded from the smaller change in  $m$  value, which is superior to that of the dense HEA. Clearly, the changes in  $m$  value in the nanochannel HEA and the dense HEA are radiation damage dependent. As shown in Fig. 5, the increment in  $S$  values in the nanochannel HEA is much lower than that of dense HEA. These results demonstrate that nanochannel structures in the nanochannel HEA can greatly reduce the defects concentration, and further alleviate the irradiation-induced embrittlement.

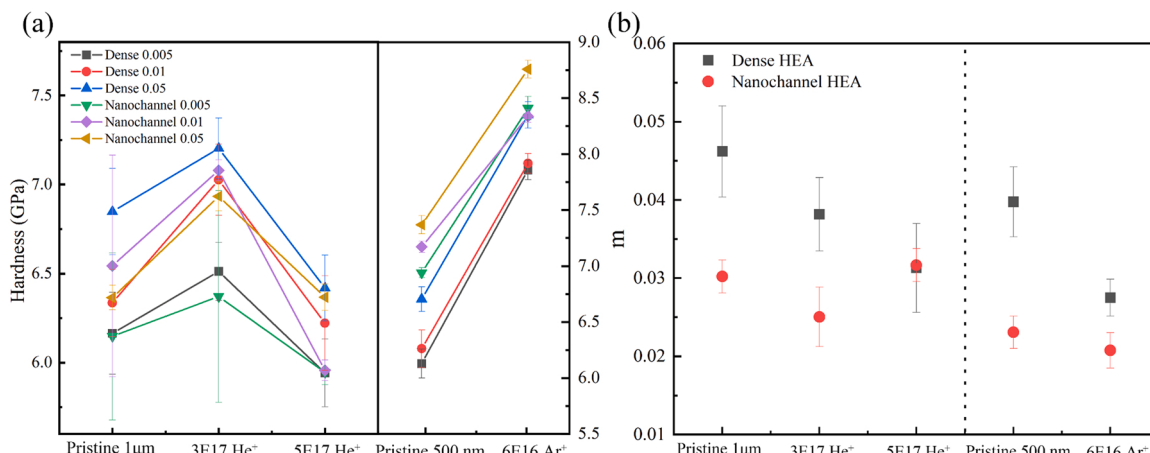


**Fig. 6.** (a) Nanoindentation hardness under different strain rates ( $0.005, 0.01$  and  $0.05 \text{ s}^{-1}$ ) and (b) SRS exponent ( $m$ ) variations of the nanochannel HEA and dense HEA before and after irradiation by  $40 \text{ keV He}^+$  ions to the fluences of  $3 \times 10^{17}$  and  $5 \times 10^{17}$  ions/ $\text{cm}^2$  and  $2 \text{ MeV Ar}^+$  ions to a fluence of  $6 \times 10^{16}$  ions/ $\text{cm}^2$ .

For the  $\text{He}^+$  ion irradiation, the pinning effect of the formed He clusters or bubbles on glide dislocation is the main cause of the hardening of the HEA films [47]. However, at the fluences of  $3 \times 10^{17}$  and  $5 \times 10^{17}$  ions/cm<sup>2</sup>, the hardness performances of the HEA films are quite different, mainly because that the smaller He bubbles in columnar grain interior can serve as strong obstacles to pinning glide dislocations, accelerating the HEA films hardening at the fluence of  $3 \times 10^{17}$  ions/cm<sup>2</sup>. However, there is a decrease in hardness at the fluence of  $5 \times 10^{17}$  ions/cm<sup>2</sup>, which is speculated to be mainly due to the heat induced by irradiation softening the film. There will be some intrinsic defects in the film deposition process due to different deposition parameters, affecting the internal stress and hardness of the film. Pang et al. observed softening of  $\text{UO}_2$  film irradiated by  $\text{Kr}^+$  ions to the fluence of  $1 \times 10^{15}$  ions/cm<sup>2</sup> at room temperature, and the hardness of the irradiated  $\text{UO}_2$  film at high temperature was significantly lower than that of the unirradiated film, indicating that heating can reduce the hardness of the film [48].

Notably, the reduction of the  $m$  value of the nanochannel HEA is less than that of dense HEA at low fluence, and the  $m$  value of nanochannel HEA does not decrease continuously but increases at high fluence. The substantial difference between the nanochannel HEA and the dense HEA is that the nanochannel HEA contains a large number of nanochannels (free surfaces), while the dense HEA does not. Free surfaces in the material have been proved that can absorb and subsequently annihilate the defects induced by irradiation, thus leading to the greatly reduced defects concentration in the matrix [47,49]. In addition, there have been a lot of researches on the reduction of SRS caused by neutron irradiation in ferrous steels and alloys, as reviewed in Ref. [50]. Therefore, the extent of elevated  $m$  value brought about by high pressure He bubbles in dense HEA may be reduced due to irradiation-induced other defects. This suggests that  $\text{He}^+$  ion irradiation leads to two competing effects on the SRS exponent: one is that high pressure He bubbles elevate the  $m$  value, while the presence of irradiated-induced other defects reduces the  $m$  value. The ruling effect depends on how the contribution of He bubbles compared with that of irradiated-induced other defects. The elevated  $m$  value observed in the  $\text{He}^+$  ion irradiated nanochannel HEA in this work suggests that nanochannels can greatly reduce the defects concentration in a matrix and transform He bubbles from a liability to an asset.

#### 4. Conclusion

Nanochannel  $\text{Al}_{0.1}\text{CoCrFeNi}$  high-entropy alloy, which contains a nanochannel structure, was fabricated. Owing to its unique nanochannel structure, the nanochannel HEA exhibits better radiation damage tolerance and He management ability than its dense counterpart. The nanochannel HEA also has a better mechanical response than its dense counterpart after both  $\text{Ar}^+$  and  $\text{He}^+$  ion irradiation. The nanochannel structure with rich free surfaces can act as “sinks” to effectively trap and annihilate irradiation-induced defects or irradiation-introduced He atoms. Astonishingly, the nanochannel structures can transform the irradiation-introduced He bubbles from a disadvantage to an asset to greatly elevate the SRS of the nanochannel HEA, which indicates improved plasticity of the nanochannel HEA.

#### CRediT authorship contribution statement

**T. Cheng:** Methodology, Validation, Formal analysis, Investigation, Writing – original draft, Visualization. **W.J. Qin:** Methodology, Formal analysis, Investigation, Data curation, Writing – original draft, Visualization. **H. Wang:** Methodology, Investigation, Data curation, Writing – original draft. **G.X. Cai:** Methodology, Visualization. **S.X. Jin:** Methodology, Formal analysis. **Y.Q. Wang:** Resources, Visualization. **C.Z. Jiang:** Resources, Visualization. **F. Ren:** Conceptualization, Resources, Writing – review & editing, Supervision, Funding acquisition.

#### Declaration of Competing Interest

The authors declare that they have no known competing financial interests or personal relationships that could have appeared to influence the work reported in this paper.

#### Acknowledgments

This work was supported by the National Natural Science Foundation of China (grants 11935011, 12105206, 11905058, and 11522543), the Natural Science Foundation of Hubei Province, China (grants 2020CFA041, 2016CFA080), the SPC-Lab Research Fund (WDZC202001) and the Fundamental Research Funds for the Central Universities (2042022kf1184) for financial support. This work was performed, in part, at the Center for Integrated Nanotechnologies, an Office of Science User Facility operated for the U.S. Department of Energy (DOE) Office of Science, Los Alamos National Laboratory, an affirmative action equal opportunity employer, is managed by Triad National Security, LLC for the U.S. Department of Energy's NNSA, under contract 89233218CNA000001.

#### Appendix A. Supporting information

Supplementary data associated with this article can be found in the online version at doi:10.1016/j.mtcomm.2023.105346.

#### References

- [1] G.S. Was, D. Petti, S. Ukai, S. Zinkle, Materials for future nuclear energy systems, J. Nucl. Mater. 527 (2019), 151837.
- [2] X.-M. Bai, A.F. Voter, R.G. Hoagland, M. Nastasi, B.P. Uberuaga, Efficient annealing of radiation damage near grain boundaries via interstitial emission, Science 327 (2010) 1631–1634.
- [3] E. Martínez, B.P. Uberuaga, I.J. Beyerlein, Interaction of small mobile stacking fault tetrahedra with free surfaces, dislocations, and interfaces in Cu and Cu-Nb, Phys. Rev. B 93 (2016), 054105.
- [4] M. Hong, Y. Wang, F. Ren, H. Zhang, D. Fu, B. Yang, X. Xiao, C. Jiang, Helium release and amorphization resistance in ion irradiated nanochannel films, EPL (Europhys. Lett.) 106 (2014) 12001.
- [5] S.-q Xia, Z. Wang, T.-f Yang, Y. Zhang, Irradiation behavior in high entropy alloys, J. Iron Steel Res. Int. 22 (2015) 879–884.
- [6] C. Wang, C.L. Tracy, S. Park, J. Liu, F. Ke, F. Zhang, T. Yang, S. Xia, C. Li, Y. Wang, Y. Zhang, W.L. Mao, R.C. Ewing, Phase transformations of Al-bearing high-entropy alloys  $\text{Al}_x\text{CoCrFeNi}$  ( $x = 0, 0.1, 0.3, 0.75, 1.5$ ) at high pressure, Appl. Phys. Lett. 114 (2019), 091902.
- [7] Y. Lu, H. Huang, X. Gao, C. Ren, J. Gao, H. Zhang, S. Zheng, Q. Jin, Y. Zhao, C. Lu, T. Wang, T. Li, A promising new class of irradiation tolerant materials:  $\text{Ti}_2\text{ZrHfV}_{0.5}\text{Mo}_{0.2}$  high-entropy alloy, J. Mater. Sci. Technol. 35 (2019) 369–373.
- [8] M. Wang, Y. Lu, T. Wang, C. Zhang, Z. Cao, T. Li, P.K. Liaw, A novel bulk eutectic high-entropy alloy with outstanding as-cast specific yield strengths at elevated temperatures, Scr. Mater. 204 (2021), 114132.
- [9] M. Wang, Y. Lu, G. Zhang, H. Cui, D. Xu, N. Wei, T. Li, A novel high-entropy alloy composite coating with core-shell structures prepared by plasma cladding, Vacuum 184 (2021), 109905.
- [10] D. Miracle, J. Miller, O. Senkov, C. Woodward, M. Uchic, J. Tiley, Exploration and development of high entropy alloys for structural applications, Entropy 16 (2014) 494–525.
- [11] C. Lu, L. Niu, N. Chen, K. Jin, T. Yang, P. Xiu, Y. Zhang, F. Gao, H. Bei, S. Shi, M. R. He, I.M. Robertson, W.J. Weber, L. Wang, Enhancing radiation tolerance by controlling defect mobility and migration pathways in multicomponent single-phase alloys, Nat. Commun. 7 (2016) 13564.
- [12] T. Yang, S. Xia, W. Guo, R. Hu, J.D. Poplawsky, G. Sha, Y. Fang, Z. Yan, C. Wang, C. Li, Y. Zhang, S.J. Zinkle, Y. Wang, Effects of temperature on the irradiation responses of  $\text{Al}_{0.1}\text{CoCrFeNi}$  high entropy alloy, Scr. Mater. 144 (2018) 31–35.
- [13] T.-n Yang, C. Lu, G. Velisa, K. Jin, P. Xiu, Y. Zhang, H. Bei, L. Wang, Influence of irradiation temperature on void swelling in  $\text{NiCoFeCrMn}$  and  $\text{NiCoFeCrPd}$ , Scr. Mater. 158 (2019) 57–61.
- [14] O. El-Atwani, N. Li, M. Li, A. Devaraj, E. Martinez, Outstanding radiation resistance of tungsten-based high entropy alloys, Sci. Adv. 5 (2019) eaav2002.
- [15] N.A.P.K. Kumar, C. Li, K.J. Leonard, H. Bei, S.J. Zinkle, Microstructural stability and mechanical behavior of  $\text{FeNiMnCr}$  high entropy alloy under ion irradiation, Acta Mater. 113 (2016) 230–244.
- [16] W. Qin, F. Ren, R.P. Doerner, G. Wei, Y. Lv, S. Chang, M. Tang, H. Deng, C. Jiang, Y. Wang, Nanochannel structures in W enhance radiation tolerance, Acta Mater. 153 (2018) 147–155.

- [17] W. Qin, F. Ren, J. Zhang, X. Dong, Y. Feng, H. Wang, J. Tang, G. Cai, Y. Wang, C. Jiang, Helium retention in krypton ion pre-irradiated nanochannel W film, *Nucl. Fusion* 58 (2018), 026021.
- [18] G. Wei, J. Li, Y. Li, H. Deng, C. Jiang, F. Ren, A better nanochannel tungsten film in releasing helium atoms, *J. Nucl. Mater.* 532 (2020), 152044.
- [19] T. Cheng, W. Qin, Y. Lian, X. Liu, J. Tang, G. Cai, S. Zhang, X. Le, C. Jiang, F. Ren, High transient-thermal-shock resistant nanochannel tungsten films, *Nanomaterials* 11 (2021) 2663.
- [20] R.E. Stoller, M.B. Toloczko, G.S. Was, A.G. Certain, S. Dwaraknath, F.A. Garner, On the use of SRIM for computing radiation damage exposure, *Nucl. Instrum. Methods Phys. Res. Sect. B Beam Interact. Mater. At.* 310 (2013) 75–80.
- [21] T. Yang, W. Guo, J.D. Poplawsky, D. Li, L. Wang, Y. Li, W. Hu, M.L. Crespillo, Z. Yan, Y. Zhang, Y. Wang, S.J. Zinkle, Structural damage and phase stability of Al0.3CoCrFeNi high entropy alloy under high temperature ion irradiation, *Acta Mater.* 188 (2020) 1–15.
- [22] I. Petrov, P. Barna, L. Hultman, J.E. Greene, S. Technology A: vacuum, films, *Microstruct. Evol. Film. Growth* 21 (2003) S117–S128.
- [23] H. Zhang, F. Ren, M. Hong, X. Xiao, G. Cai, C. Jiang, Structure and growth mechanism of V/Ag multilayers with different periodic thickness fabricated by magnetron sputtering deposition, *J. Mater. Sci. Technol.* 30 (2014) 1012–1019.
- [24] J.T. Gudmundsson, D. Lundin, Introduction to magnetron sputtering, in: *High Power Impulse Magnetron Sputtering*, Elsevier, 2020, pp. 1–48.
- [25] D. Chen, Y. Tong, H. Li, J. Wang, Y.L. Zhao, A. Hu, J.J. Kai, Helium accumulation and bubble formation in FeCoNiCr alloy under high fluence He<sup>+</sup> implantation, *J. Nucl. Mater.* 501 (2018) 208–216.
- [26] F. Granberg, K. Nordlund, M.W. Ullah, K. Jin, C. Lu, H. Bei, L.M. Wang, F. Djurabekova, W.J. Weber, Y. Zhang, Mechanism of radiation damage reduction in equiatomic multicomponent single phase alloys, *Phys. Rev. Lett.* 116 (2016), 135504.
- [27] S. Taller, G.S. Was, Understanding bubble and void nucleation in dual ion irradiated T91 steel using single parameter experiments, *Acta Mater.* 198 (2020) 47–60.
- [28] D. Chen, N. Li, D. Yuryev, J.K. Baldwin, Y. Wang, M.J.J.Sa Demkowicz, Self-organization of helium precipitates into elongated channels within metal nanolayers, 3 (2017) eaao2710.
- [29] J. Tang, M. Hong, Y. Wang, W. Qin, F. Ren, L. Dong, H. Wang, L. Hu, G. Cai, C. Jiang, Microstructural evolution of nanochannel CrN films under ion irradiation at elevated temperature and post-irradiation annealing, *J. Nucl. Mater.* 500 (2018) 242–251.
- [30] H. Zhang, F. Ren, Y. Wang, M. Hong, X. Xiao, D. Liu, W. Qin, X. Zheng, Y. Liu, C. Jiang, Enhanced radiation tolerance of nanochannel V films through defects release, *Nucl. Instrum. Methods Phys. Res. Sect. B Beam Interact. Mater. At.* 334 (2014) 1–7.
- [31] J. Cízek, Characterization of lattice defects in metallic materials by positron annihilation spectroscopy: a review, *J. Mater. Sci. Technol.* 34 (2018) 577–598.
- [32] M. Sćepanović, V. de Castro, I. García-Cortés, F.J. Sánchez, T. Gigl, C. Hugenschmidt, T. Leguey, Characterisation of open volume defects in Fe–Cr and ODS Fe–Cr alloys after He<sup>+</sup> and Fe<sup>+</sup> ion irradiations, *J. Nucl. Mater.* 538 (2020), 152230.
- [33] W. Qin, S. Jin, X. Cao, Y. Wang, P. Peres, S.-Y. Choi, C. Jiang, F. Ren, Influence of nanochannel structure on helium-vacancy cluster evolution and helium retention, *J. Nucl. Mater.* 527 (2019), 151822.
- [34] W. Qin, Y. Wang, M. Tang, F. Ren, Q. Fu, G. Cai, L. Dong, L. Hu, G. Wei, C. Jiang, Microstructure and hardness evolution of nanochannel W films irradiated by helium at high temperature, *J. Nucl. Mater.* 502 (2018) 132–140.
- [35] A. Rida, M. Micoulaut, E. Rouhaud, A. Makke, Understanding the strain rate sensitivity of nanocrystalline copper using molecular dynamics simulations, *Comput. Mater. Sci.* 172 (2020) 207–222.
- [36] H. Wang, P. Wu, S. Kurukuri, M.J. Worswick, Y. Peng, D. Tang, D. Li, Strain rate sensitivities of deformation mechanisms in magnesium alloys, *Int. J. Plast.* 107 (2018) 207–222.
- [37] X. Feng, J.U. Surjadi, X. Li, Y. Lu, Size dependency in stacking fault-mediated ultrahard high-entropy alloy thin films, *J. Alloy. Compd.* 844 (2020) 264–277.
- [38] X. Feng, J. Zhang, Y. Wang, Z. Hou, K. Wu, G. Liu, J. Sun, Size effects on the mechanical properties of nanocrystalline NbMoTaW refractory high entropy alloy thin films, *Int. J. Plast.* 95 (2017) 264–277.
- [39] J.Y. Zhang, G. Liu, J. Sun, Strain rate effects on the mechanical response in multi- and single-crystalline Cu micropillars: grain boundary effects, *Int. J. Plast.* 50 (2013) 1–17.
- [40] Q. Wei, S. Cheng, K.T. Ramesh, E. Ma, Effect of nanocrystalline and ultrafine grain sizes on the strain rate sensitivity and activation volume: fcc versus bcc metals, *Mater. Sci. Eng. A* 381 (2004) 71–79.
- [41] S. Gangireddy, B. Gwalani, R.S. Mishra, Grain size dependence of strain rate sensitivity in a single phase FCC high entropy alloy Al0.3CoCrFeNi, *Materials Science and Engineering: A*, 736 (2018) 344–348.
- [42] N.-R. Kang, E.-J. Gwak, H. Jeon, E. Song, J.-Y. Kim, Microstructural effect on time-dependent plasticity of nanoporous gold, *Int. J. Plast.* 109 (2018) 108–120.
- [43] A.T. Jennings, J. Li, J.R. Greer, Emergence of strain-rate sensitivity in Cu nanopillars: transition from dislocation multiplication to dislocation nucleation, *Acta Mater.* 59 (2011) 5627–5637.
- [44] Z.W. Shan, R.K. Mishra, S.A. Syed Asif, O.L. Warren, A.M. Minor, Mechanical annealing and source-limited deformation in submicrometre-diameter Ni crystals, *Nat. Mater.* 7 (2008) 115–119.
- [45] H. Zheng, A. Cao, C.R. Weinberger, J.Y. Huang, K. Du, J. Wang, Y. Ma, Y. Xia, S. X. Mao, Discrete plasticity in sub-10-nm-sized gold crystals, *Nat. Commun.* 1 (2010) 144.
- [46] A. Kunz, S. Pathak, J.R. Greer, Size effects in Al nanopillars: Single crystalline vs. bicrystalline, *Acta Mater.* 59 (2011) 4416–4424.
- [47] W. Qin, Y. Wang, M. Tang, F. Ren, Q. Fu, G. Cai, L. Dong, L. Hu, G. Wei, C. Jiang, Microstructure and hardness evolution of nanochannel W films irradiated by helium at high temperature, *J. Nucl. Mater.* 502 (2018) 132–140.
- [48] M.S. Elbakshwan, Y. Miao, J.F. Stubbins, B.J. Heuser, Mechanical properties of UO<sub>2</sub> thin films under heavy ion irradiation using nanoindentation and finite element modeling, *J. Nucl. Mater.* 479 (2016) 548–558.
- [49] H. Wang, F. Ren, J. Tang, W. Qin, L. Hu, L. Dong, B. Yang, G. Cai, C. Jiang, Enhanced radiation tolerance of YSZ/Al2O3 multilayered nanofilms with pre-existing nanovoids, *Acta Mater.* 144 (2018) 691–699.
- [50] N. Kumar, A. Alsabbagh, C. Seok, K. Murty, *Synergistic Effects of Neutron Irradiation and Interstitial Nitrogen on Strain Aging in Ferritic Steels*, in: *Mechanical and Creep Behavior of Advanced Materials*, Springer, 2017, pp. 151–164.